Revealing the interplay between the structural complexity of triphenylamine redox derivatives and their charge transport processes via computational modeling

Robert Herzhoff,[a] Fabrizia Negri,[b] Klaus Meerholz,[a] Daniele Fazzi [b]

[a]Institut für Physikalische Chemie, Department für Chemie, Universität zu Köln, Greinstr. 4-6, 50939 Köln, Germany.

[b]Università di Bologna, Dipartimento di Chimica 'Giacomo Ciamician', Via F. Selmi, 2, 40126 Bologna, Italy.

Supporting Information

Table of Contents

Force field parametrization

In this work, the OPLS-AA [1,2] force field parameters for **TPA**, **TPD**, **FTPD** and *spiro*-**OMeTAD** were refined using *ab initio* methods. The procedure is detailed for **TPA** in the following. From the structure optimized at the DFT (ωB97X-D/6-311G*) level, the equilibrium bond distances and dihedral angles were obtained, while the charges were calculated via CHELPG. The force field parameters for the three *identical and correlated* dihedral angles in **TPA** were then determined via the following procedure. One dihedral angle was scanned at the DFT (ωB97X-D/6-311G*) level while the others were allowed to relax. The same scan was repeated at the MD level with the dihedral angle parameters set to zero. Here, the two dihedral angles that were not being scanned were fixed at their QM determined minimum position. The resulting energies of the DFT and MD scan were subtracted from each other, and the resulting potential profile was fitted with the Ryckaert-Bellemans function

$$V_{rb}(\varphi) = \sum_{n=0}^{5} V_n \cos^n \varphi \qquad (1)$$

where φ is the dihedral angle, yielding the desired dihedral angle parameters V_n (see Table S1). The procedure was repeated analogously for **TPD**, **FTPD** and *spiro*-**OMeTAD**. In Figure S1, the defined atom types for **TPA**, **TPD** and **FTPD** are shown. The atom types and angles for *spiro*-**OMeTAD** largely correspond to those of **FTPD**, which is why only the central spiro-bifluorene core is shown.
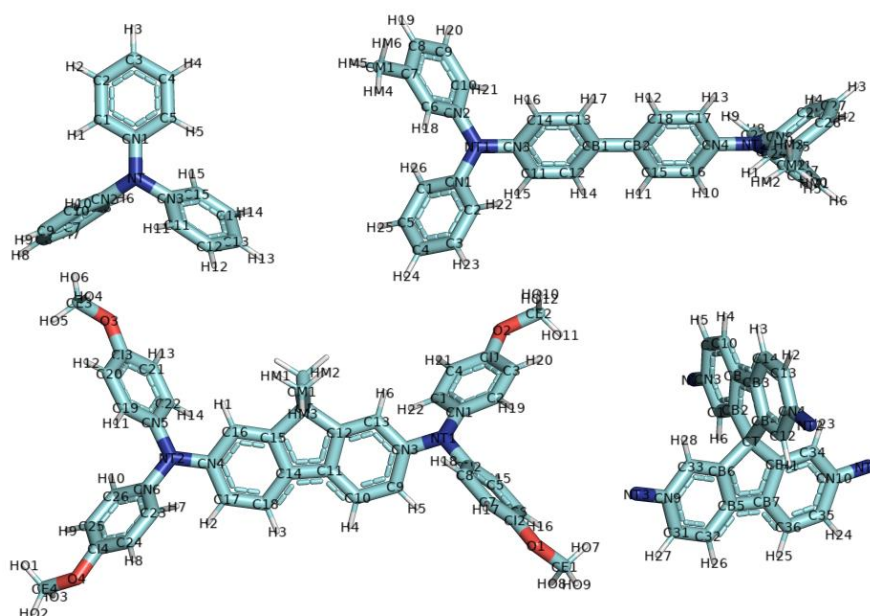
Figure S1: Atom types for **TPA**, **TPD**, and **FTPD**. The atom types and angles for *spiro*-**OMeTAD** mostly correspond to those of **FTPD**, which is why only the central spiro-bifluorene core is shown.

In Figure S2 the dihedral angle profiles of **TPA**, **TPD** and **FTPD** at the DFT, initial and refined MD level are shown together with the dihedral angle distribution in the amorphous bulk phases. For *spiro-OMeTAD*, the dihedral parameters of **FTPD** were used directly, and only the dihedral angle distribution is shown. The Ryckaert-Bellemans parameters of the dihedral angles are given in Table S1.
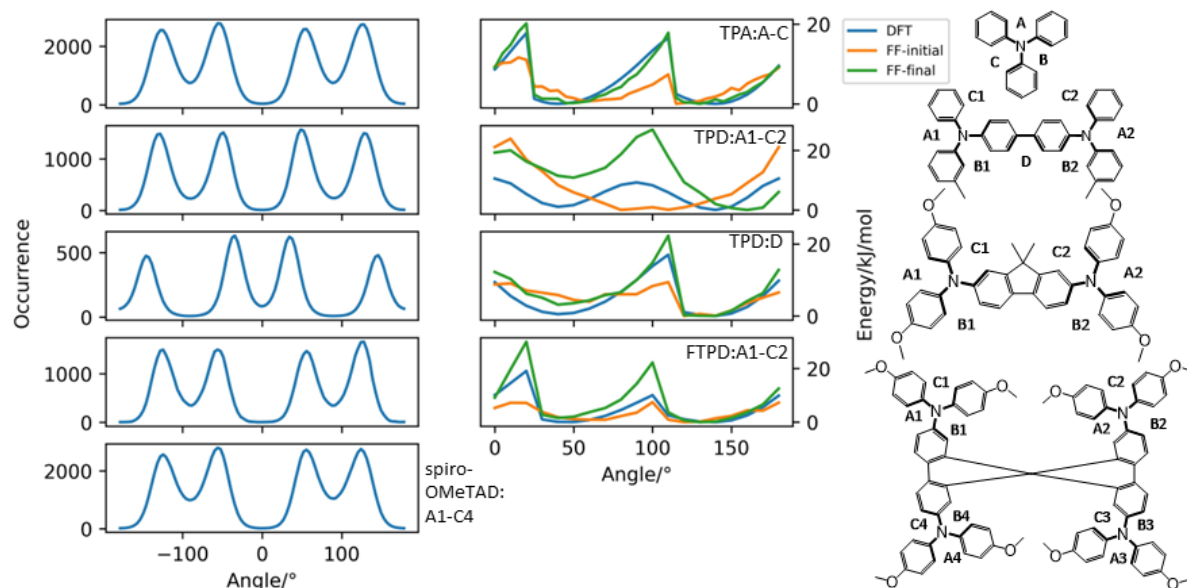
Figure S2: Left panels: dihedral angle distribution in the amorphous bulk phase. Right panels: dihedral angle potential energy profiles at the DFT (ωB97X-D/6-311G*) level and from the initial and final force field. Dihedral angles are indicated in the chemical structures on the right side.

Table S1: Ryckaert-Bellemans parameters $(V_n, \frac{kJ}{mol})$ for the dihedral angles in **TPA**, **TPD** and **FTPD**. For *spiro-OMeTAD*, the **FTPD** values were used. **A-C** refers to the dihedral angles between atoms CN-NT-CN-C, **D** refers to the dihedral angle between atoms C-CB-CB-C and **E** refers to the dihedral angle between the atoms C-CI-O-CE.

|	V_0	V_1	V_2	V_3	V_4	V_5
TPA:A-C	4.271	0.000	-8.499	0.000	4.469	0.000
TPD:A1-C2	0.152	-14.59	-18.08	23.43	14.22	-11.62
TPD:D	8.589	0.463	-32.30	-11.63	13.86	8.602
FTPD:A1-C2	1.850	-0.350	-10.27	-0.837	9.705	1.867
FTPD:E	4.405	1.665	1.995	-7.289	-10.85	4.864

Amorphous morphology simulation

With the refined force field parameters at hand, amorphous morphologies were simulated with a thermal annealing approach, similar to reports in literature. [3] First, 125 molecules were placed randomly in a box by PACKMOL. [4] Subsequently, an energy minimization was performed using a steepest descent algorithm. The system was then equilibrated in the NVT ensemble at 700 K for 1 ns, followed by NVT equilibration at 300 K for 1 ns. Lastly, NPT equilibration at 300 K was performed until convergence of the density. The system was then extended in a 2x2x2 supercell containing 1000 molecules, and the previous procedure was repeated, extending the last NPT run until the density converged. All molecular dynamics simulations were performed in periodic boundary conditions using the GROMACS [5–9] program package. For temperature control, velocity rescaling with an additional stochastic term was applied (τ_T = 0.2 ps), while for the pressure, isotropic coupling with a Berendsen barostat was applied (p_{ref} = 1.01325 bar, τ_T = 0.5 ps, compressibility = $4.5 \cdot 10^{-5}$ bar^{-1}). A 1 fs timestep was used in all simulations as well as a 10 Å cut-off radius for the van-der-Waals and Coulombic interactions. The PME method with a 0.12 nm Fourier spacing was used for electrostatic interactions.

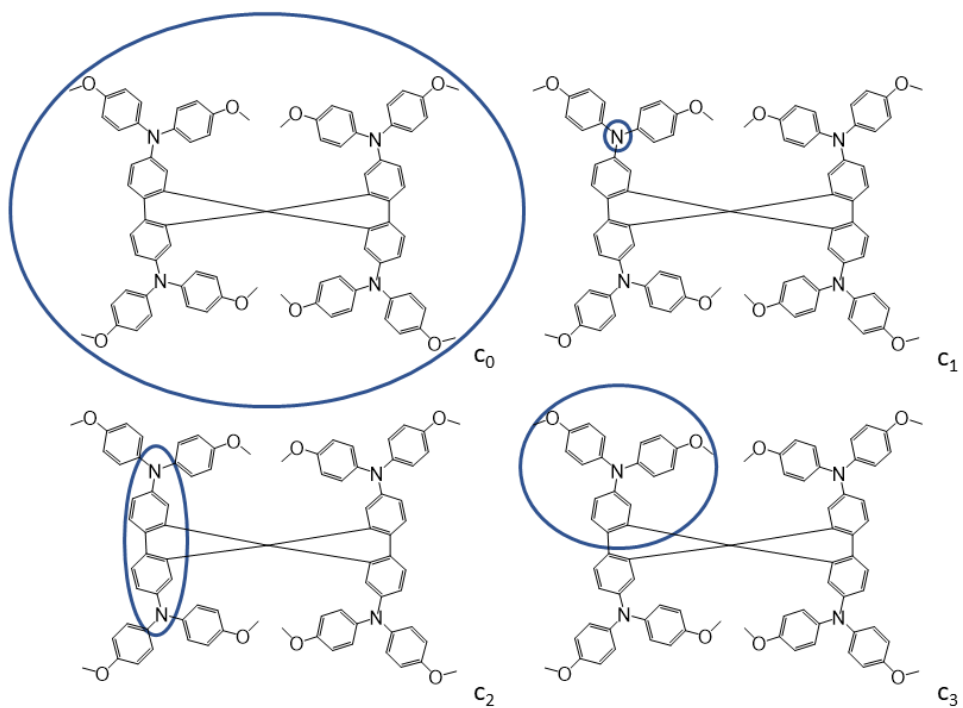## Charged state geometric parameters
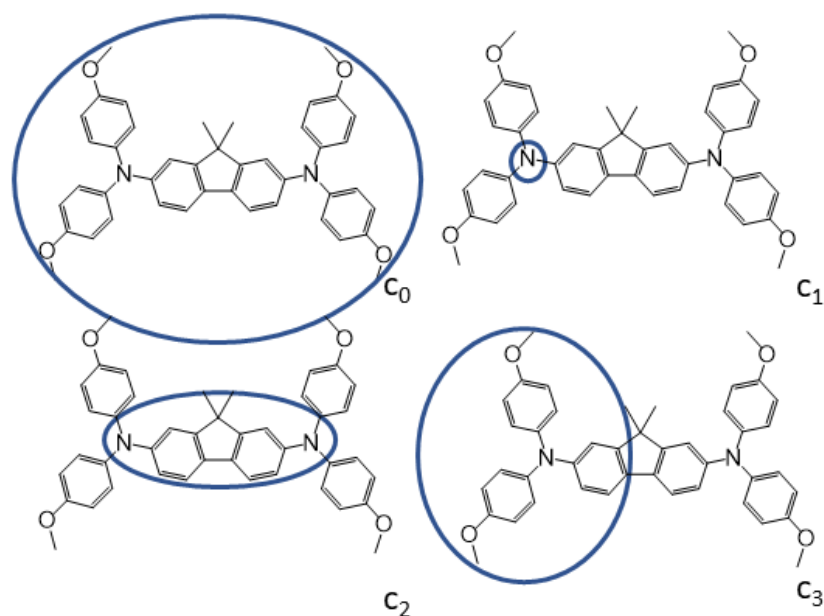
Figure S3: Charge constrain schemes for **FTPD**. The circles indicate the area where the positive charge is localized.
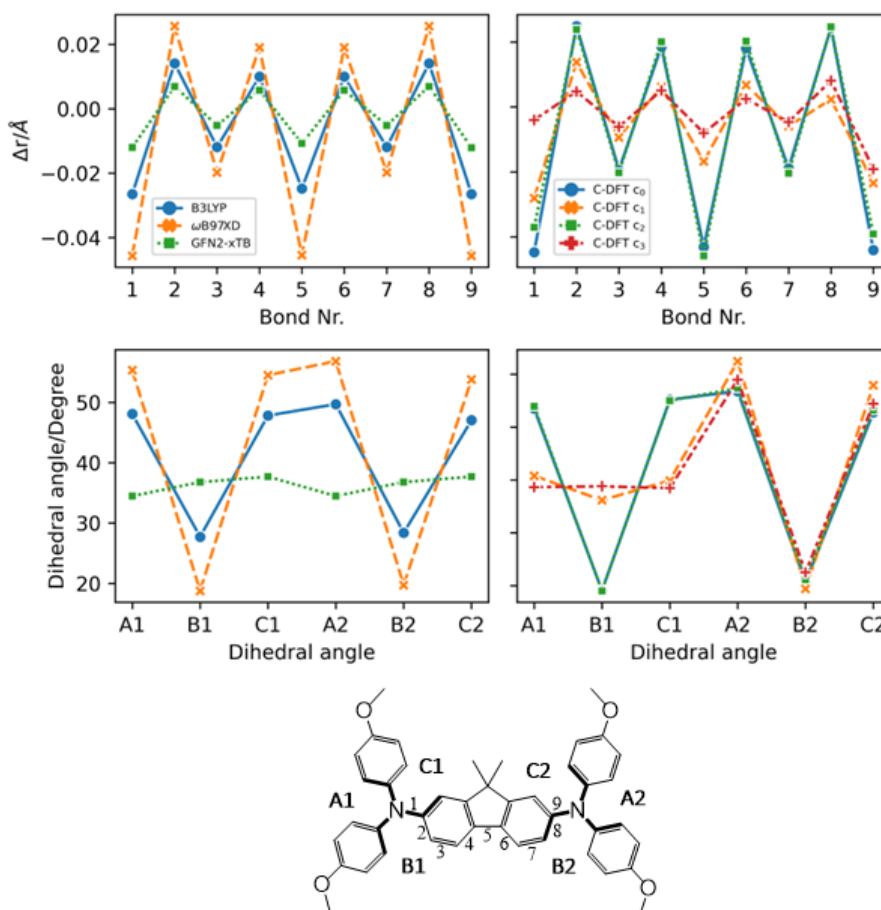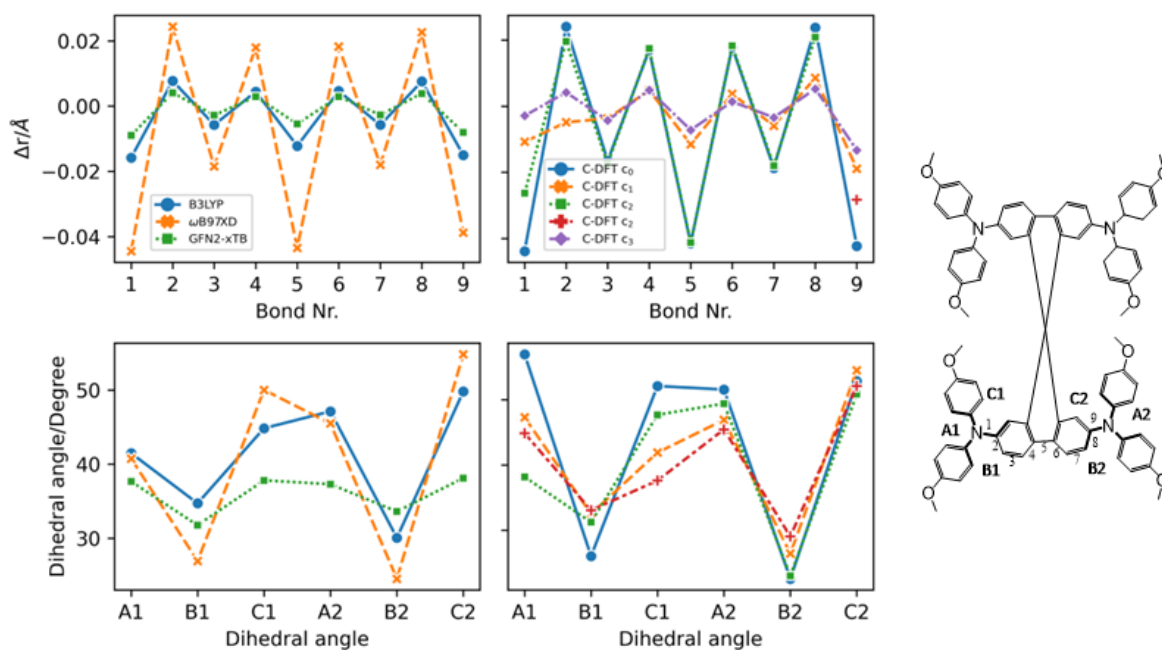
Figure S4: Geometric parameters of **FTPD** in the charged state (+1) by considering different methods (DFT, C-DFT, GFN2-xTB), DFT functionals and various charge constraint (C-DFT) schemes. The two panels on the top show the bond length difference ($\Delta r = r_{charged} - r_{neutral}$) patterns by moving from the neutral to the charged state. Top left panel: DFT (B3LYP, ωB97X-D) and GFN2-xTB data. Top right panel: C-DFT data with different schemes. The two panels on the bottom show the dihedral angles in the charged state. Bottom left panel: DFT (B3LYP, ωB97X-D) and GFN2-xTB data. Bottom right panel: C-DFT data with different charge constraint schemes.

Localizing the charge on one half of the molecule has different effects on **FTPD** when compared with **TPD** (Figure 4). The rigid bridge of **FTPD** leads to a larger reorganization energy in constrain scheme c_3 because the entire bridge reacts to the charged state reorganization instead of just one phenyl unit. On the other hand, the discrepancy between the methods is not as large for **FTPD** because the rigid fluorene unit cannot assume a staggered conformation preventing the delocalization like **TPD**. The bond length alternation patterns also show the impact of the charge delocalization mainly in the bond length of bond 5, which corresponds to the central bond of the bridging unit in both **TPD** and **FTPD**. This bond is significantly shortened if the charge is allowed to delocalize over the central bridging unit due to π-conjugation.

Figure S5: Charge constrain schemes for *spiro*-**OMeTAD**. The circles indicate the area where the positive charge is localized.

Figure S6: Geometric parameters of **_spiro_-OMeTAD** in the charged state (+1) by considering different methods (DFT, C-DFT, GFN2-xTB), DFT functionals and various charge constraint (C-DFT) schemes. The two panels on the top show the bond length difference ($\Delta r = r_{charged} - r_{neutral}$) patterns by moving from the neutral to the charged state. Top left panel: DFT (B3LYP vs. ωB97X-D) versus GFN2-xTB data. Top right panel: C-DFT data with different schemes. The two panels on the bottom show the dihedral angles in the charged state. Bottom left panel: DFT (B3LYP vs. ωB97X-D) versus GFN2-xTB data. Bottom right panel: C-DFT data with different charge constraint schemes.

For **_spiro_-OMeTAD**, the observations with regard to the bond length alternation patterns and the changes in the dihedral angles are largely consistent with **FTPD**, even though the asymmetric changes in dihedral angles due to charge localization are less pronounced due to the steric demands of the overall bulkier structure.

Electronic coupling and geometric data
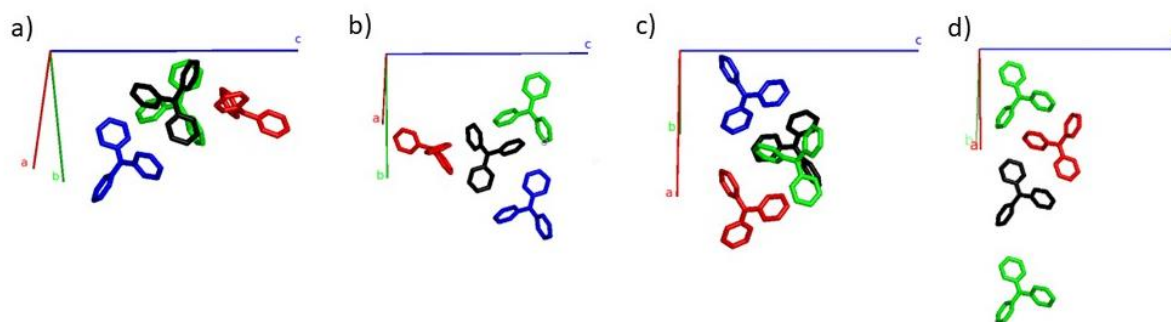
Figure S7: Selected pairs with large electronic coupling for the four unique monomers of the **TPA** unit cell with the crystallographic axes. The four unique centers are shown in black and the neighbours forming the different pairs with the black centers are shown in red, green or blue. The pair formed with the red neighbour has the highest electronic coupling, followed by the green and blue neighbour.

Table S2: Electronic coupling and geometric data for the pairs shown in **Fig. S7(a).** Pair A refers to the pair formed from the black and red monomers, pair B to the pair formed from the black and green monomers and pair C to the pair formed from the black and blue monomers.

	J_{ij}/meV	ΔCoM/Å	ΔCoM x/Å	ΔCoM y/Å	ΔCoM z/Å
A(red)	50	6.56	1.13	0.16	6.46
B(green)	37	5.49	-3.73	4.03	-0.20
C(blue)	34	7.36	5.24	2.72	-4.39

Table S3: Electronic coupling, transfer rates and geometric data for the pairs shown in **Fig. S7(b).**

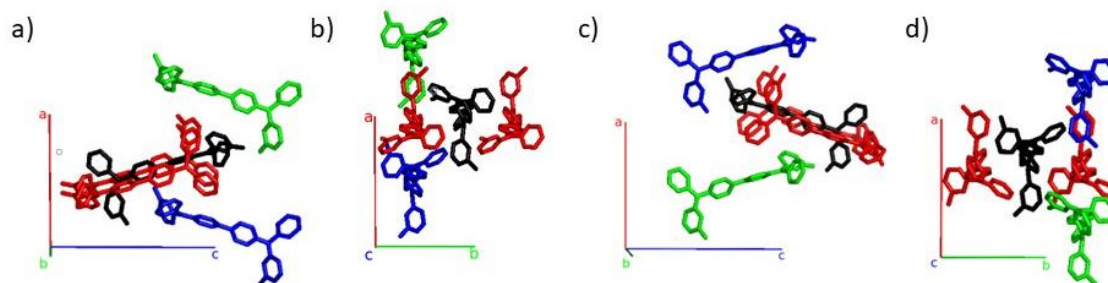|	J_{ij}/meV	ΔCoM/Å	ΔCoM x/Å	ΔCoM y/Å	ΔCoM z/Å
A(red)	50	6.56	-1.13	0.16	-6.46
B(green)	40	7.15	-5.05	-2.55	4.37
C(blue)	36	7.36	2.7	5.27	4.37

Table S4: Electronic coupling, transfer rates and geometric data for the pairs shown in **Fig. S7(c).**

	J_{ij}/meV	ΔCoM/Å	ΔCoM x/Å	ΔCoM y/Å	ΔCoM z/Å
A(red)	40	7.15	5.05	2.55	-4.37
B(green)	37	5.49	3.73	-4.03	0.2
C(blue)	36	7.36	-2.7	-5.27	-4.37

Table S5: Electronic coupling and geometric data for the pairs shown in **Fig. S7(d).**

|	J_{ij}/meV	ΔCoM/Å	ΔCoM x/Å	ΔCoM y/Å	ΔCoM z/Å
A(red)	34	7.36	-5.24	-2.72	4.39
B(green)	10	11.01	-7.75	-7.82	0
C(blue)	10	11.01	7.75	7.82	0

Figure S8: Selected pairs with large electronic coupling for the two unique monomers of the **TPD** unit cell with the crystallographic axes. The two unique centers are shown in black and the neighbours forming the different pairs with the black centers are shown in red, green or blue. The pair formed with the red neighbour has the highest electronic coupling, followed by the green and blue neighbour.

Table S6: Electronic coupling and geometric data for the pairs shown in **Fig. S8(a)/(b).** Pair A refers to the pair formed from the black and red monomers, pair B to the pair formed from the black and green monomers and pair C to the pair formed from the black and blue monomers.

	J_{ij}/meV	ΔCoM/Å	ΔCoM x/Å	ΔCoM y/Å	ΔCoM z/Å
A1(red)	36	6.13	-0.83	-5.51	-2.56
A2(red)	36	6.13	-0.83	5.51	-2.56
B(green)	11	11.06	7.22	-5.43	6.39
C(blue)	8	11.06	-7.22	-5.43	6.39

Table S7: Electronic coupling and geometric data for the pairs shown in **Fig. S8(c)/(d).**

	J_{ij}/meV	ΔCoM/Å	ΔCoM x/Å	ΔCoM y/Å	ΔCoM z/Å
A1(red)	35	6.12	-1.02	-5.51	2.47
A2(red)	35	6.12	-1.02	5.51	2.47
B(green)	11	11.06	-7.22	5.43	-6.39
C(blue)	8	11.06	7.22	5.43	-6.39
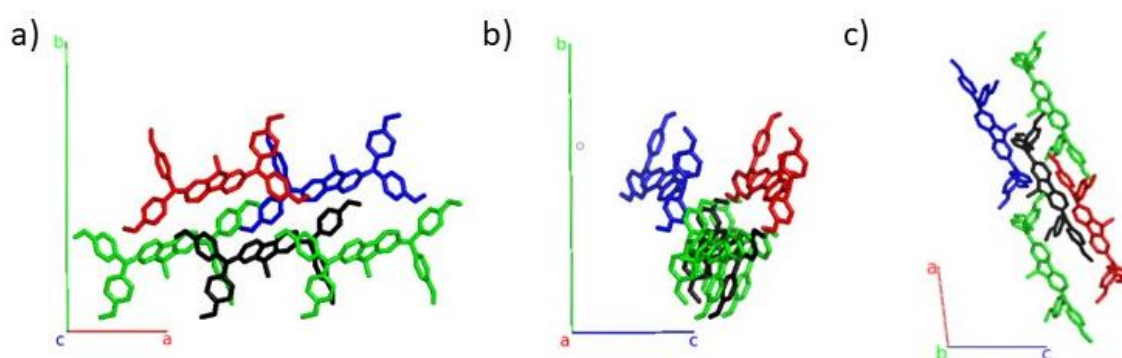
Figure S9: Selected pairs with large electronic coupling for the unique monomer of the **FTPD** unit cell with the crystallographic axes. The unique center is shown in black and the neighbours forming the different pairs with the black centers are shown in red, green or blue. The pair formed with the red neighbour has the highest electronic coupling, followed by the green and blue neighbour.

Table S8: Electronic coupling and geometric data for the pairs shown in **Fig. S9(a)/(b)/(c).**

|	J_{ij}/meV	ΔCoM/Å	ΔCoM x/Å	ΔCoM y/Å	ΔCoM z/Å
A(red)	9.8	11.00	-5.25	7.77	5.75
B1(green)	9.3	9.96	-9.96	0	0
B2(green)	9.3	9.96	9.96	0	0
C(blue)	9.0	11.85	6.3	7.77	-6.34
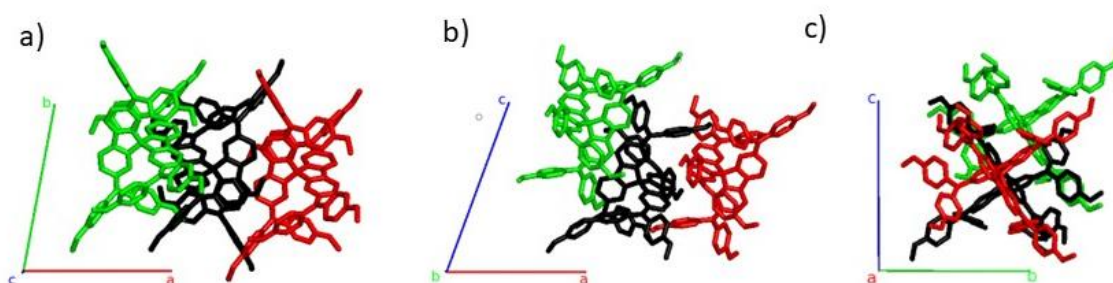
Figure S10: Selected pairs with large electronic coupling for the unique monomer of the *spiro*-**OMeTAD** unit cell with the crystallographic axes. The unique center is shown in black and the neighbours forming the different pairs with the black centers are shown in red, green or blue. The pair formed with the red neighbour has the highest electronic coupling, followed by the green neighbour.

Table S9: Electronic coupling and geometric data for the pairs shown in **Fig. S10 (a)/(b)/(c).**

	J_{ij}/meV	ΔCoM/Å	ΔCoM x/Å	ΔCoM y/Å	ΔCoM z/Å
A(red)	39	8.58	7.44	0.545	4.24
B(green)	15	7.55	-6.22	0.545	4.24

Kinetic Monte-Carlo charge transport simulations (zero-field) in the amorphous phase
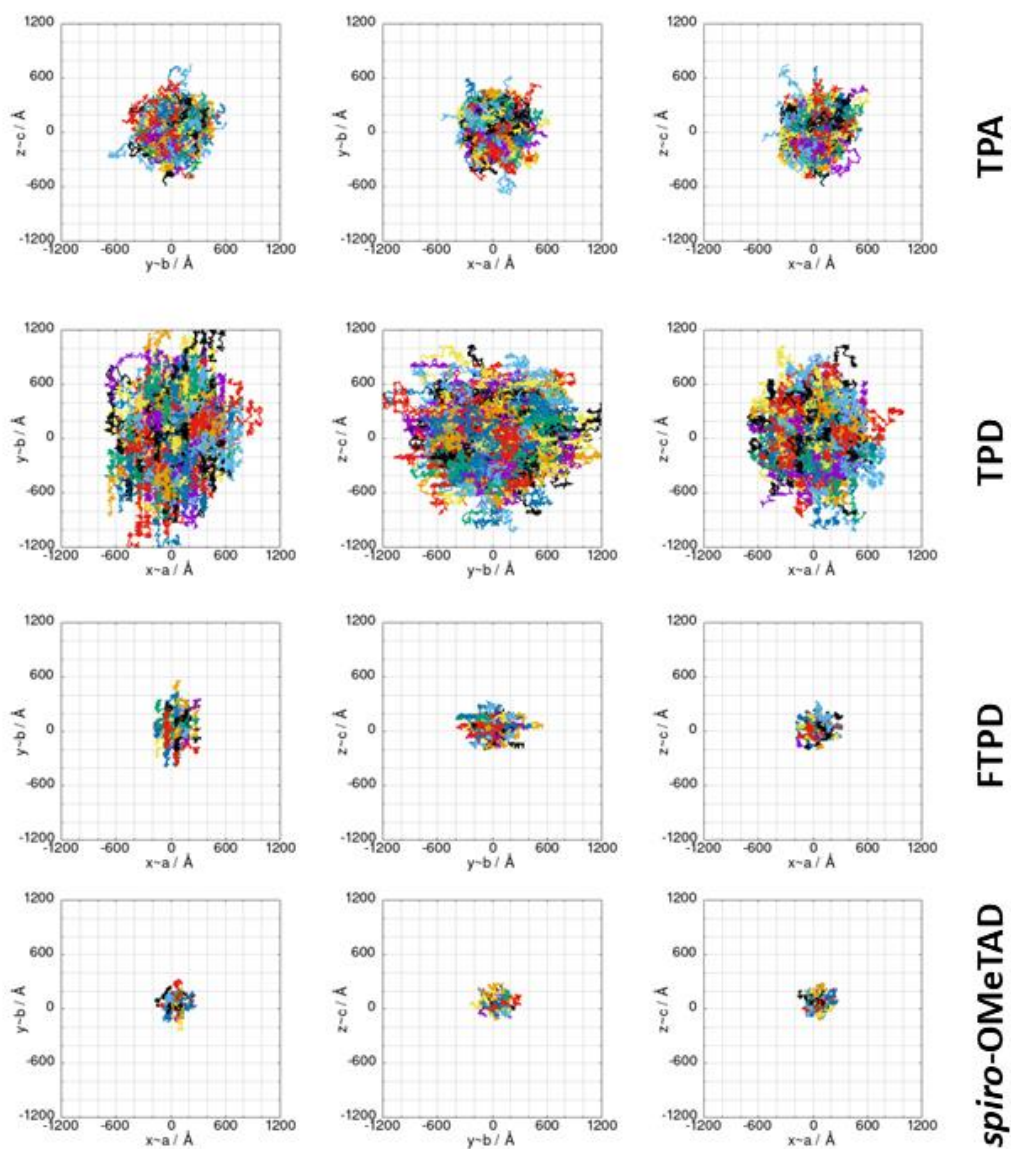
Figure S11: KMC trajectories computed in amorphous phases (zero-field) shown from different planes. The colors used in the plots only serve to discern the superimposed trajectories.

Charge mobilities with an applied electric field

Table S10: Mobilities $(\mu, \frac{cm^2}{Vs})$ in the crystalline and amorphous phases in x- y- and z- directions with an electric field of $10^8 \frac{V}{m}$. For these simulations, in the amorphous case, just one snapshot of the MD-simulated systems was used.

	TPA	TPD	FTPD	*spiro*-OMeTAD
Crystalline, μ_x	$4.68 \cdot 10^{-2}$	$3.88 \cdot 10^{-3}$	$6.07 \cdot 10^{-3}$	$3.98 \cdot 10^{-2}$
Crystalline, μ_y	$4.82 \cdot 10^{-2}$	$2.97 \cdot 10^{-1}$	$2.53 \cdot 10^{-3}$	$4.04 \cdot 10^{-3}$
Crystalline, μ_z	$3.57 \cdot 10^{-2}$	$1.25 \cdot 10^{-2}$	$3.42 \cdot 10^{-4}$	$8.04 \cdot 10^{-4}$
Amorphous, μ_x	$8.61 \cdot 10^{-3}$	$5.98 \cdot 10^{-3}$	$1.48 \cdot 10^{-4}$	$4.17 \cdot 10^{-5}$
Amorphous, μ_y	$8.71 \cdot 10^{-3}$	$5.72 \cdot 10^{-3}$	$1.34 \cdot 10^{-4}$	$3.93 \cdot 10^{-5}$
Amorphous, μ_z	$7.81 \cdot 10^{-3}$	$5.70 \cdot 10^{-3}$	$8.41 \cdot 10^{-5}$	$5.08 \cdot 10^{-6}$
Experimental	$2 \cdot 10^{-2}$ [10] (single crystal)	$1 \cdot 10^{-3}$ [11] (amorphous thin film)	$4.3 \cdot 10^{-4}$ [12] (semicrystalline thin film)	$1.30 \cdot 10^{-3}$ [13] (single crystal) $1.69 \cdot 10^{-6}$ [13] (amorphous thin film)

Computed dielectric constants

The dielectric constants ε_s were computed based on the Clausius-Mosotti relation [14]

$$\varepsilon_s = 1 + \frac{12\pi\alpha \frac{N}{V}}{3 - 4\pi\alpha \frac{N}{V}} \qquad (2)$$

with α being the molecular polarizability volume, N being the number of particles and V being the volume of the simulation boxes.

Table S11: Computed dielectric constants.

	TPA	TPD	FTPD	*spiro*-OMeTAD
ε_s(amorphous)	2.19	1.87	1.99	2.09
ε_s(crystal)	2.42	2.49	2.50	2.70

**Low CoM distance pair in the amorphous phase of FTPD**
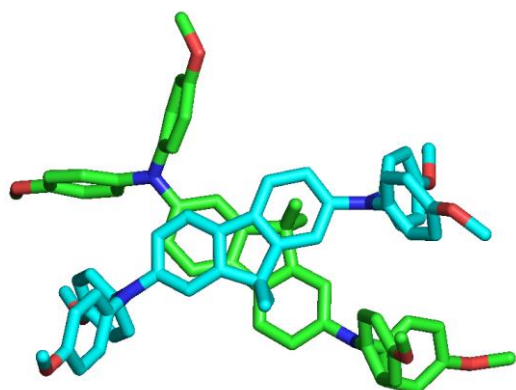
Figure S12: Pair with low CoM distance in the amorphous phase of **FTPD**, taken from the MD-production run. The crossed conformation of the long molecular axes of the pair leads to lower CoM distance values compared to the crystalline phase.

BLYP35/6-311G* hole reorganization energies

Table S12: Internal hole reorganization energy (λ_{int}, eV) calculated at the BLYP35/6-311G* level. In these calculations, imaginary frequencies were encountered which is why they were not used in further simulations, however are still reported here for reference.

	TPA	TPD	FTPD	*spiro*-OMeTAD
BLYP35	0.13	0.46	0.34	0.31

Electronic coupling distribution (extended)
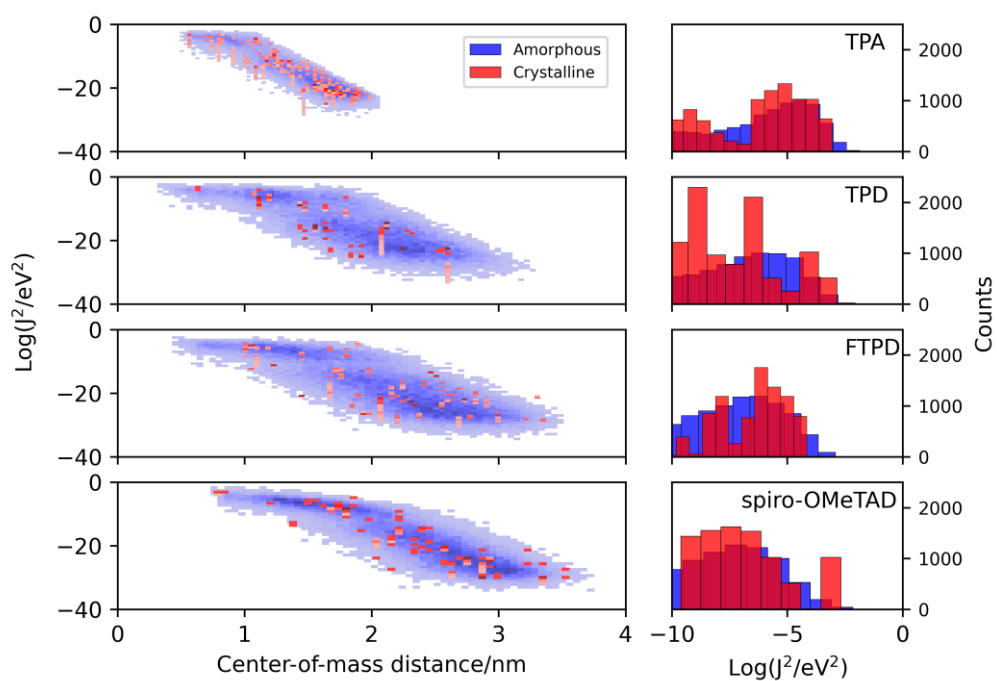
Figure S13: Coupling integral distributions ($Log(J_{ij}^2/eV^2)$) as calculated with the MOO approach versus center-of-mass (CoM) distance in experimental crystalline (red) and MD generated amorphous (blue) phases, left panels. The right panel shows the coupling integral histograms up to -10 $Log(J^2/eV^2)$, i.e., up to 10^{-5} eV, for both amorphous (blue) and crystalline (red) phases.

Computed and experimental hole mobility
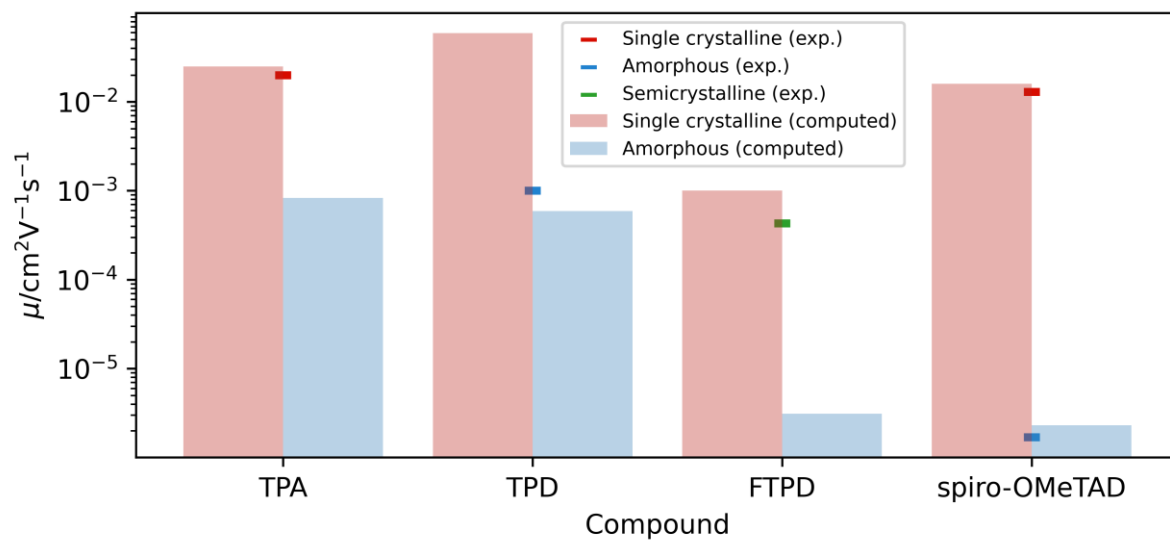
Figure S14: Computed (average) and experimental[10,11,12,13] hole mobility in the crystalline and amorphous phases.

References

1   W. L. Jorgensen, D. S. Maxwell and J. Tirado-Rives, *J. Am. Chem. Soc.*, 1996, **118**, 11225–11236.

2   G. A. Kaminski, R. A. Friesner, J. Tirado-Rives and W. L. Jorgensen, *J. Phys. Chem. B*, 2001, **105**, 6474–6487.

3   K.-H. Lin, A. Prlj, L. Yao, N. Drigo, H.-H. Cho, M. K. Nazeeruddin, K. Sivula and C. Corminboeuf, *Chem. Mater.*, 2019, **31**, 6605–6614.

4   L. Martínez, R. Andrade, E. G. Birgin and J. M. Martínez, *J. Comput. Chem.*, 2009, **30**, 2157–2164.

5   H. Berendsen, D. van der Spoel and R. van Drunen, *Comput. Phys. Commun.*, 1995, **91**, 43–56.

6   B. Hess, C. Kutzner, D. van der Spoel and E. Lindahl, *J. Chem. Theory Comput.*, 2008, **4**, 435–447.

7   E. Lindahl, B. Hess and D. van der Spoel, *J. Mol. Model.*, 2001, **7**, 306–317.

8   S. Pronk, S. Páll, R. Schulz, P. Larsson, P. Bjelkmar, R. Apostolov, M. R. Shirts, J. C. Smith, P. M. Kasson, D. van der Spoel, B. Hess and E. Lindahl, *Bioinformatics*, 2013, **29**, 845–854.

9   D. van der Spoel, E. Lindahl, B. Hess, G. Groenhof, A. E. Mark and H. J. C. Berendsen, *J. Comput. Chem.*, 2005, **26**, 1701–1718.

10 D. C. Hoesterey and G. M. Letson, *J. Chem. Phys.*, 1964, **41**, 675–679.

11 M. Stolka, J. F. Yanus and D. M. Pai, *J. Phys. Chem.*, 1984, **88**, 4707–4714.

12 L. Fang, A. Zheng, M. Ren, X. Xie and P. Wang, *ACS Appl. Mater. Interfaces*, 2019, **11**, 39001–39009.

13 D. Shi, X. Qin, Y. Li, Y. He, C. Zhong, J. Pan, H. Dong, W. Xu, T. Li, W. Hu, J.-L. Brédas and O. M. Bakr, *Sci. Adv.*, 2016, **2**, e1501491.

14 R. P. Feynman, R. B. Leighton and M. Sands, *Lectures on Physics: Commemorative Issue*, Addison Wesley, Reading, MA, 2nd edn., 1971.